Application of the generalised fully Lagrangian approach to simulating polydisperse gas-droplet flows

Y. Li [a], O. Rybdylova [b,*]

[a] *Department of Earth Sciences, University of Oxford, Oxford OX1 3AN, UK*
[b] *Advanced Engineering Centre, School of Computing, Engineering and Mathematics, University of Brighton, Brighton BN2 4GJ, UK*

ARTICLE INFO

ABSTRACT

In this paper, we demonstrate the application of a generalised fully Lagrangian approach to the simulation of polydisperse gas-evaporating droplet flows. The paper focuses on the proposed methodology for modelling the dispersed phase, droplets, in both steady and transient cases. To account for polydispersity, the set of Lagrangian variables is extended to include the droplet size, and the droplet size distribution function is introduced to the droplet parameter set. According to the Lagrangian approach, all the droplet parameters, including the distribution function, are found along the droplet trajectories. An interpolation scheme to convert droplet parameter fields from a Lagrangian to an Eulerian framework for visualising droplet distribution is proposed. The developed methodology was applied to simple 1D and 2D stationary cases for verification, after which it was incorporated into OpenFOAM to simulate steady and periodic flows around a cylinder. In the case of a steady flow, a region devoid of droplets is formed behind the cylinder. From the droplet distribution plots, it was observed that small and medium sized droplets reach a region near to the axis of the symmetry of the flow. In the case of periodic flow, the analysis of droplet distribution is based on instantaneous pictures of the droplet parameters rather than their values along droplet trajectories. In this flow, strongly influenced by vortices, a strong droplet segregation is shown; at various locations one can see a full droplet size spectrum, only small or large droplets, and/or droplets from a narrow size interval. In all cases, the effect of the evaporation is to decrease the maximum value of the droplet distribution function shifted towards smaller-sized droplets.

1. Introduction

Two-phase flows, more specifically gas-droplet flows, are widespread in daily life, for example aerosols generated when coughing and sneezing (Bourouiba et al., 2014), and in applications, for example aerosol drug delivery (Dolovich and Dhand, 2011), and sprays in gasoline engines (Panão and Moreira, 2004). The fundamental physics involved is essentially the interaction between a dispersed phase of droplets and a carrier phase, that includes not only momentum exchange, but also heat transport and phase change in some applications.

One aim of relevant studies within this topic is to understand the concentration of the dispersed phase within the carrier phase and the mechanisms leading to accumulation and scattering of the droplets. There are many experimental studies of sprays, including those that provide information about droplet sizes and their velocities, see for example Begg et al. (2009) and Dunbar et al. (1975). However, it is difficult to reconstruct instantaneous droplet distribution fields from

their experimental data. Thus, there is a great interest in the development of mathematical and numerical models for theoretical studies which have the potential to provide insight into the phenomena. Examples of such works include those by Almeida and Jaberi (2006) and Karchniwy et al. (2019), where various patterns of droplets clustering according to their sizes were identified by simulating evaporating polydisperse sprays in turbulent flows. Segregation of droplets by sizes within a laminar oscillating flow was demonstrated by Greenberg and Katoshevski (2016).

While the carrier phase is usually modelled using the classic Navier–Stokes equations (Eulerian approach), there are two approaches that describe the dispersed phase. One is based on the assumption that the cloud of droplets is a continuum, and the equations for the dispersed phase are derived in the Eulerian framework (see for example Laurent and Massot, 2001; Laurent et al., 2004). This is known as the Eulerian–Eulerian (EE) approach. The other method is based on tracking each droplet or a parcel of identical droplets along their trajectories (see for

example Almeida and Jaberi, 2006; Karchniwy et al., 2019). This is called the Eulerian–Lagrangian (EL) approach. Both EE and EL approaches have their advantages and disadvantages, and it is now well-known when, or in which cases, it is preferable to use one rather than the other. See for example Laurent and Massot (2001) for a case where EE is more computationally efficient than EL. On the other hand, EE requires careful consideration when dealing with the intersection of droplet trajectories, which leads to multi-valued fields of droplet velocities. In this case, the standard EL modelling method can accurately reveal the dynamics of each individual droplet, however the computational costs are higher than for the EE approach if droplet concentration needs to be evaluated and then a great number of particles have to be tracked for the sake of accuracy, for example as reviewed by Healy and Young (2005).

In an effort to mitigate the drawback of the EL method, two different approaches were proposed, one by Fernandez et al. (1981) and the other by Osiptsov (2000), by incorporating the assumption of droplet phase continuity into the original EL method. Healy and Young (2005) reported that Osiptsov's approach benefits from not only elegance and simplicity in its mathematical form but also greater accuracy and can be applied to numerically generated flow fields. Osiptsov's approach will be used in this work, and is here referred to as the fully Lagrangian approach (FLA).

Previous studies have demonstrated the capability of the FLA to model monodisperse droplets in a carrier phase which is described either analytically (Osiptsov, 2000; Rybdylova et al., 2016; 2018) or numerically (Zaripov et al., 2017; 2018; Papoutsakis et al., 2018). Some authors have also included the evaporation models of droplets together with the FLA (Zaripov et al., 2017; 2018). However, there is still a lack of development of the FLA for simulating a polydisperse two-phase flow, though Osiptsov (2000) proposed a mathematical formulation of a generalised FLA for this purpose. To the best of our knowledge, there are no works on actual application of the generalised FLA for evaporating polydisperse flows.

Polydisperse gas-droplet flows with evaporation have previously been modelled using the EE (for example Laurent and Massot, 2001; Laurent et al., 2004; Dagan et al., 2017; Tambour, 1984; Greenberg et al., 1993) and the EL approaches (for example Almeida and Jaberi, 2006; Karchniwy et al., 2019; Tambour, 1985). In the sectional approach, the droplet size domain is divided into a number of sections and it is assumed that the total number of droplets within each section, taking into account fluxes to the adjacent sections, is conserved (Tambour, 1984). Due to its design it is more convenient to use this approach with the EE model because it does not require the tracking of particular trajectories, although some attempts have been made to also couple it with an EL model (see for example Tambour, 1985). Another method, called the sampling approach, is based on defining a number of samples within the size domain then tracking each one as an independent group of monodisperse droplets. The sampling approach is mostly used in EL models.

In this paper, we demonstrate the application of the generalised FLA to simple 1D and 2D steady cases as well as its implementation to OpenFOAM to simulate evaporating polydisperse droplets in a hot gas. It is envisaged that the generalised FLA will build on the strengths of the original FLA, when all droplet parameters, including number density, are calculated from a system of ordinary differential equations, and provide a complete picture of droplet distribution in terms of size, space and time. Coupling of the generalised FLA with OpenFOAM will enable more advanced modelling, which will be illustrated using an example of periodic flow past a cylinder. Finally, for a complete analysis, it is essential to plot droplet number density distribution in space; we have developed and proposed an interpolation scheme to map the results from the Lagrangian onto the Eulerian framework.

When considering polydisperse droplet flows, it is certainly expected that one will observe the size segregation of droplets depending on their initial size and velocity distribution, as shown in Karchniwy et al.

(2019). While we recognise that it would be an interesting direction of study to explore the effect of initial droplet distribution on spatial and temporal droplet concentration fields, this is out of the scope of this paper, which focuses upon the methodology and its practical implementation for CFD studies.

The paper is structured as follows. Section 2 is dedicated to the formulation of the problem, including the full list of assumptions used in the development of the model and a brief description of the original FLA. The details of the generalised FLA and its application to the 1D and 2D steady state cases are presented in Section 3. Implementation of the generalised FLA and its application to flow around a cylinder are described in Section 4. The results of the work are summarised in Section 5. Technical details about the mesh, time step, domain, and verification of the implemented FLA in OpenFOAM using an analytical solution are included in the Appendices.

2. Mathematical formulation

2.1. Eulerian–Lagrangian framework

The general physical problem of interest in this work is a flow of gas loaded with evaporating droplets, where the size of the droplets is not uniform across the droplet cloud. The problem is considered in the framework of the one-way coupled two-fluid approach (Marble, 1970). The one-way coupled approach is applicable to dilute sprays with a negligibly low mass loading of droplets. In this study, the Eulerian–Lagrangian approach is adopted. The carrier phase is described using the Eulerian approach, i.e. Navier–Stokes equations. In the case studies discussed in the paper, it is assumed that the carrier phase is a viscous incompressible gas. However, the focus of the paper is on the methodology for the dispersed phase, for which no assumptions are required with regard to the carrier phase. Hence, the methodology can be applied to compressible flows without limitations.

To describe the dynamics of such two-phase systems within the Eulerian–Lagrangian framework with conventional Lagrangian tracking, the governing equations for a non-evaporating case can be written in the following dimensionless form:

$$\left(\frac{\partial}{\partial t} + \mathbf{u}_g \cdot \nabla\right)\mathbf{u}_g = -\nabla p + \frac{1}{\text{Re}}\nabla^2 \mathbf{u}_g, \quad \text{Re} = \frac{\rho_g U L}{\mu_g}, \tag{1}$$

$$\nabla \cdot \mathbf{u}_g = 0, \tag{2}$$

$$\frac{d\mathbf{x}_d}{dt} = \mathbf{u}_d, \tag{3}$$

$$\frac{d\mathbf{u}_d}{dt} = \mathbf{f}_d. \tag{4}$$

The force $\mathbf{f}_d$ is usually a known function of velocity and size (Crowe et al., 2011). Note, that it is assumed that the droplets are much larger than the molecular size so that Brownian motion can be ignored. The flow is laminar and the volumetric fraction of droplets is negligibly small, so that the dispersed media is a 'cold gas' without stresses (Marble, 1970). In System (1)–(4), $\mathbf{x}$ and $\mathbf{u}$ are the radius vector and velocity normalised by L and U respectively, the subscripts g and d are applied to distinguish between the variables of the gas and droplet phases respectively. ρ_g and μ_g denote the density and viscosity of the gas, other notations are conventional, U, L are the chosen scales of velocity and length used for nondimensionalisation of the governing equations. The time scale can then be determined as L/U. Here and in what follows, the equations and results are presented and discussed in dimensionless forms unless otherwise stated.

2.2. Standard fully Lagrangian approach

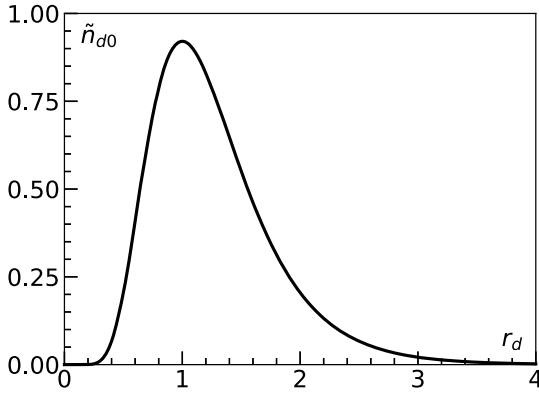According to the fully Lagrangian approach (FLA) (Osiptsov, 2000),

Fig. 1. Initial distribution $\widetilde{n}_{d0}$ as defined by the Eq. (11).

the droplet phase is a continuum, and the Lagrangian variables are droplet initial locations $\mathbf{x}_{d0}$, and time. The number density n_d along chosen trajectories is calculated from the continuity equation taken in the Lagrangian form, which is based on the deformation of the local element with respect to its initial state.

For monodisperse droplets without evaporation, Eqs. (3) and (4) are complemented by the following equations, which are required for number density calculations:

$$n_d = \frac{n_{d0}}{|det\mathbf{J}|}, \quad \text{where} \quad J_{ij} = \frac{\partial x_{d,i}}{\partial x_{d0,j}}, \quad \mathbf{x}_d = (x_d, y_d, z_d), \tag{5}$$

$$\frac{dJ_{ij}}{dt} = \frac{\partial u_{d,i}}{\partial x_{d0,j}} = \omega_{ij}, \quad \text{where} \quad \mathbf{u}_d = (u_{d,x}, u_{d,y}, u_{d,z}), \tag{6}$$

$$\frac{d\omega_{ij}}{dt} = \frac{\partial}{\partial x_{d0,j}} \frac{du_{d,i}}{dt} = \frac{\partial}{\partial x_{d0,j}} f_{d,i},$$

$$\text{where} \quad \mathbf{f}_d = (f_{d,x}, f_{d,y}, f_{d,z}). \tag{7}$$

Here, $\mathbf{J}$ is the Jacobian of the transformation from Lagrangian to Eulerian coordinates. The subscript $d0$ is used to denote the initial values of the droplet parameters.

3. Generalisation of the FLA for the case of evaporating polydisperse droplets

The model described in Section 2.2 can be generalised for the case of polydisperse droplets (Osiptsov, 2000). The set of Lagrangian variables is extended to include the initial droplet size, thus the full set of Lagrangian variables is x_{d0}, y_{d0}, z_{d0}, and r_{d0}, where r_{d0} is the initial droplet radius. The continuity equation for the dispersed phase is generalised to

$$\widetilde{n}_d(t, \mathbf{x}_{d0}, r_{d0})|det\mathbf{J}| = \widetilde{n}_{d0}. \tag{8}$$

Here, $\widetilde{n}_d$ is a distribution function of droplets along their trajectories, which depends not only on $\mathbf{x}_{d0}$ and t, but on r_{d0} also. $\mathbf{J}$ is the Jacobian of the transformation from Lagrangian to Eulerian coordinates with the following components:

$$\mathbf{J} = \begin{pmatrix} J_{11} & J_{12} & J_{13} & J_{14} \\ J_{21} & J_{22} & J_{23} & J_{24} \\ J_{31} & J_{32} & J_{33} & J_{34} \\ J_{41} & J_{42} & J_{43} & J_{44} \end{pmatrix}$$

$$= \begin{pmatrix} \partial x_d/\partial x_{d0} & \partial x_d/\partial y_{d0} & \partial x_d/\partial z_{d0} & \partial x_d/\partial r_{d0} \\ \partial y_d/\partial x_{d0} & \partial y_d/\partial y_{d0} & \partial y_d/\partial z_{d0} & \partial y_d/\partial r_{d0} \\ \partial z_d/\partial x_{d0} & \partial z_d/\partial y_{d0} & \partial z_d/\partial z_{d0} & \partial z_d/\partial r_{d0} \\ \partial r_d/\partial x_{d0} & \partial r_d/\partial y_{d0} & \partial r_d/\partial z_{d0} & \partial r_d/\partial r_{d0} \end{pmatrix}. \tag{9}$$

The equations for the dispersed phase are:

$$\frac{\partial \mathbf{x}_d}{\partial t} = \mathbf{u}_d, \quad \frac{\partial \mathbf{u}_d}{\partial t} = \mathbf{f}_d, \quad \frac{\partial T_d}{\partial t} = q_d, \quad \frac{\partial r_d}{\partial t} = \dot{r}_d,$$

$$\frac{\partial J_{ij}}{\partial t} = \omega_{ij}, \quad \frac{\partial \omega_{ij}}{\partial t} = \frac{\partial f_{di}}{\partial x_{d,k}} J_{kj} + \frac{\partial f_{di}}{\partial u_{d,k}} \omega_{kj} + \frac{\partial f_{di}}{\partial r_d} J_{4j},$$

$$\text{for } i, k = 1, 2, 3, \quad j = 1, \ldots, 4, \tag{10}$$

$$\frac{\partial J_{4j}}{\partial t} = \frac{\partial \dot{r}_d}{\partial x_{d,k}} J_{kj} + \frac{\partial \dot{r}_d}{\partial u_{d,k}} \omega_{kj} + \frac{\partial \dot{r}_d}{\partial r_d} J_{4j}, \quad \frac{\partial J_{44}}{\partial t}$$

$$= \frac{\partial \dot{r}_d}{\partial x_{d,k}} J_{k4} + \frac{\partial \dot{r}_d}{\partial u_{d,k}} \omega_{k4} + \frac{\partial \dot{r}_d}{\partial r_d} J_{44}, \quad j, k = 1, 2, 3.$$

Where, $\dot{r}_d$ is the rate of droplet size change, which is usually a known function of the droplet size and thermodynamic parameters as it is directly related to the droplet evaporation, q_d is the heat flux to the droplet, the values of $1, 2, 3$, and 4 correspond to x, y, z, and r respectively. On a chosen droplet trajectory, System (10) is a system of ordinary differential equations. The initial conditions correspond to how droplets are introduced into the flow. These conditions are defined in a similar way as for the original FLA (Osiptsov, 2000; Healy and Young, 2005).

3.1. Droplet distribution function

Assuming that the injection generates a polydisperse spray, we need to define the initial droplet size distribution and to find a new size distribution at a chosen location and time instance.

In the cases considered in this paper, it is assumed that the initial distribution of droplet size is the same at all initial locations $\mathbf{x}_{d0}$ and that it is log-normal:

$$\widetilde{n}_{d0} = \frac{1}{r_{d0}} \frac{1}{S\sqrt{2\pi}} \exp\left(-\frac{(\ln r_{d0} - M)^2}{2S^2}\right). \tag{11}$$

In this work, M and S take the values of 0.16 and 0.4. Such initial distribution is illustrated in the plot in Fig. 1 where $r_d = r_{d0}$, that is, a droplet radius scaled by r_{d0}^*, a reference droplet radius corresponding to the highest number of droplets.

It was demonstrated that the assumption of a log-normal distribution of droplet sizes is adequate for some applications (see for example Nguyen et al., 2016). However, this assumption does not limit the methodology described in Section 3. In fact, any form of the distribution function may be used, including a tabulated form.

To find the total number density $n_d(t, \mathbf{x})$ at a chosen location $\mathbf{x} = \mathbf{x}_p$ and time instance $t = t_p$, one needs to firstly map the distribution $\widetilde{n}_d$ from the Lagrangian to the Eulerian coordinates. If the flow is steady, n_d and $\widetilde{n}_d$ in the Eulerian framework do not vary in time, and the Lagrangian 'time' becomes a parameter along a droplet trajectory. The droplet distribution in the Eulerian framework is found as $\widetilde{n}_d(t_p, \mathbf{x}_p, r_d)$ for all sizes of droplet at this chosen location and time instance. Finally, the total number density $n_d(t_p, \mathbf{x}_p)$ is calculated by integrating $\widetilde{n}_d(t_p, \mathbf{x}_p, r_d)$ over the whole range of droplet sizes $r_d \in [r_{d,\min}, r_{d,\max}]$:

$$n_d(t_p, \mathbf{x}_p) = \int_{r_{d,\min}}^{r_{d,\max}} \widetilde{n}_d(t_p, \mathbf{x}_p, r_d) dr_d. \tag{12}$$

It should be noted that in the general case $\widetilde{n}_d(t_p, \mathbf{x}_p, r_d)$ can be discontinuous, also, it may happen that $\widetilde{n}_d = 0$ within a certain range of r_d implying that there are no droplet of the corresponding size in the location under consideration. In the case, where $\widetilde{n}_d$ is a discontinuous function of r_d at a given t_p and $\mathbf{x}_p$, one need to integrate every continuous fragment and sum them together to obtain n_d.

3.2. Application of the generalised FLA to simple cases

In this section and what follows it is assumed that the dimensional expressions for the force, heat flux and evaporation rate $\dot{m}$ for a droplet
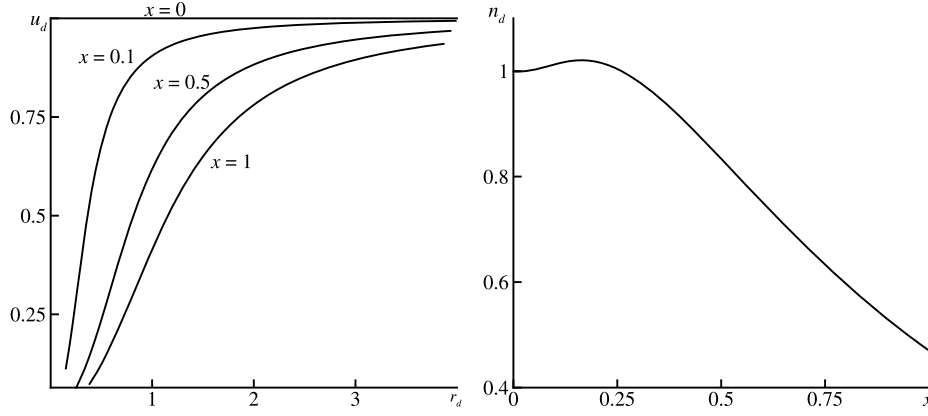
Fig. 2. Left: Distribution of droplet velocities with their sizes at cross-sections $x = 0, 0.1, 0.5$, and 1. Right: The total number density n_d along the x-axis.

are:

$$\mathbf{f}_d^* = 6\pi r_d^* \mu_g \left(\mathbf{u}_g^* - \mathbf{u}_d^* \right),$$

$$q_d^* = 4\pi r_d^* k_l \left(T_g^* - T_d^* \right), \tag{13}$$

$$\dot{m} = -\frac{q_d^*}{H}.$$

Here, the superscript $*$ represents the dimensional parameters, k_l and H denote the droplet liquid thermal conductivity and the latent heat of evaporation. These simple models for the force and heat flux are only applicable for a narrow range of flow parameters, namely small droplet Reynolds number, that $\mathrm{Re}_d = \rho_g r_d^* \left| \mathbf{u}_g^* - \mathbf{u}_d^* \right| / \mu_g \ll 1$. The expression for the evaporation rate corresponds to the case when all the heat that reaches a droplet surface is spent on its evaporation. These expressions, however, are for demonstration purposes only. The methodology presented in the paper is valid if other expressions for the force and heat flux are considered without limitations.

The dimensionless equations corresponding to expressions (13) are:

$$\frac{d\mathbf{u}_d}{dt} = \frac{1}{\mathrm{Stk}\, r_d^2} \left(\mathbf{u}_g - \mathbf{u}_d \right), \quad \mathrm{Stk} = \frac{2\rho_d r_{d0}^{*2} U}{9\mu_g L}$$

$$\frac{dT_d}{dt} = 0, \quad \frac{dr_d^2(t)}{dt} = -\delta, \quad \delta = \frac{2k_l}{\rho_d r_{d0}^{*2} H} \left(T_g^* - T_d^* \right). \tag{14}$$

Here, ρ_d is the droplet liquid density.

3.2.1. 1D stationary case of droplets evaporating into a quiescent carrier phase

Consider an injection of droplets into a still hot air with uniform temperature where the droplets are injected with a constant velocity and temperature. For this problem, the velocity scale is equal to the droplet injection velocity, U, the length scale is equal to the characteristic droplet velocity relaxation length, $L = 2\rho_d r_d^{*2} U / (9\mu_g)$, then $\mathrm{Stk} = 1$.

For a chosen droplet trajectory, we have the following system of ODEs:

$$\frac{dx_d}{dt} = u_d, \quad \frac{du_d}{dt} = -\frac{1}{r_d^2} u_d, \quad \frac{dr_d^2}{dt} = -\delta,$$

$$\frac{dJ_{11}}{dt} = \omega_{11}, \quad \frac{dJ_{12}}{dt} = \omega_{12}, \quad \frac{dJ_{21}}{dt} = 0, \quad \frac{dJ_{22}}{dt} = \frac{\delta}{2r_d^2} J_{22},$$

$$\frac{d\omega_{11}}{dt} = -\frac{1}{r_d^2}\omega_{11} + \frac{2}{r_d^3} u_d J_{21}, \quad \frac{d\omega_{12}}{dt} = -\frac{1}{r_d^2}\omega_{12} + \frac{2}{r_d^3} u_d J_{22}. \tag{15}$$

The initial conditions for System (15) are:

$$x = x_0, \quad u_d = 1, \quad \widetilde{n}_d = \widetilde{n}_{d0}, \quad r_d = r_{d0},$$
$$J_{11} = J_{22} = 1, \quad J_{12} = J_{21} = 0, \quad \omega_{11} = \omega_{12} = \omega_{21} = \omega_{22} = 0. \tag{16}$$

System (15) can be solved analytically, and was used for verification of the calculations. The solution is

$$x_d = \frac{r_{d0}^2}{\delta + 1} \left[1 - \left(1 - \frac{\delta t}{r_{d0}^2} \right)^{(\delta+1)/\delta} \right],$$

$$u_d = \left(1 - \frac{\delta t}{r_{d0}^2} \right)^{1/\delta}, \quad r_d^2 = r_{d0}^2 - \delta t,$$

$$J_{11} = 1, \quad J_{12} = -\frac{2r_{d0}}{1+\delta} \left[\left(1 - \frac{\delta t}{r_{d0}^2} \right)^{1/\delta} \left(1 + \frac{t}{r_{d0}^2} \right) - 1 \right], \tag{17}$$

$$J_{21} = 0, \quad J_{22} = \left(1 - \frac{\delta t}{r_{d0}^2} \right)^{-1/2},$$

$$\widetilde{n}_d = \widetilde{n}_{d0} \left(1 - \frac{\delta t}{r_{d0}^2} \right)^{1/2}.$$

The developed methodology enables collection of detailed information about the distribution of droplets; for example, one can plot the distribution of droplet velocities vs. their sizes (see Fig. 2 (left), $\delta = 1$). As demonstrated in the figure, smaller droplets relax to the quiescent carrier gas faster. At each point, a distribution of droplets was reconstructed and the total number density integrated. The evolution of the total number density along the axis is presented in Fig. 2 (right). The total number density increases as the droplets slow down and accumulate near the injection point. As the droplets travel downstream, they evaporate completely and disappear, which leads to a decrease in the total number density.

3.2.2. 2D stationary case: fan spray injection into a cross-flow

This case was proposed to study the effect of droplet trajectory crossing on the reconstruction of the total number density fields. Consider an injection of droplets into a hot air with a uniform temperature and a constant velocity perpendicular to the droplet injection, which forms a 90°–jet. The dimensional velocity magnitude of the gas and the droplet at injection are U and $0.8U$ respectively. The length scale and Stk are defined in the same way as in Section 3.2.1.

In the case of a 2D steady-state flow, System (10) takes form:

$$\widetilde{n}_d(t, x_{d0}, r_{d0}) \left| \det \begin{pmatrix} J_{11} & J_{12} & J_{13} \\ J_{21} & J_{22} & J_{23} \\ J_{31} & J_{32} & J_{33} \end{pmatrix} \right| = \widetilde{n}_{d0}. \tag{18}$$

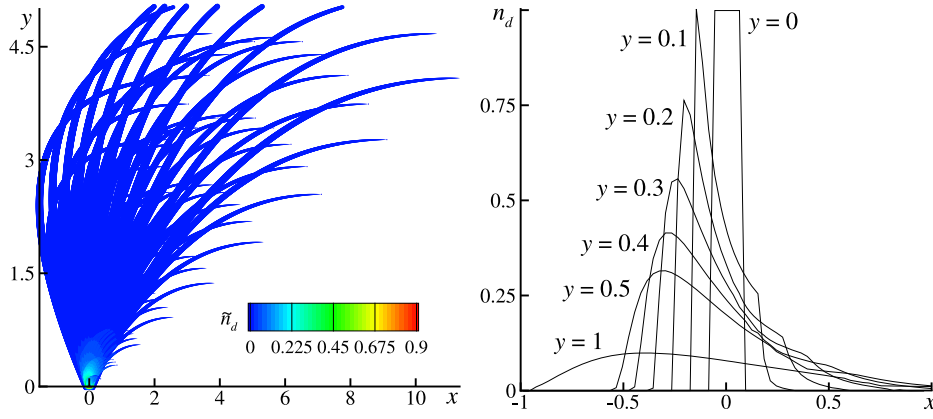For horizontal flow of the carrier phase, System (10) takes the form:

Fig. 3. Left: Droplet trajectories. Size of the markers corresponds to the size of the droplets, values of distribution function $\widetilde{n}_d$ are denoted by colour. Right: Total number density profiles at various cross-sections.
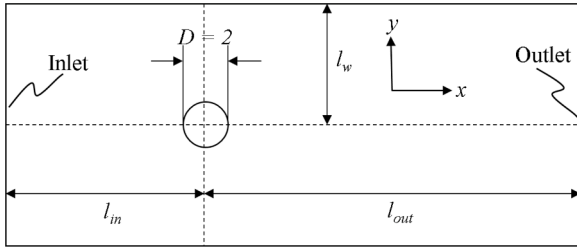

Fig. 4. The 2D computational domain of the gas flow past the circular cross-section of a cylinder with a diameter of 2.l_{in}, l_{out} and l_w represent the distance from the centre of the cylinder to the inlet boundary on the left, the outlet boundary on the right and the periodic boundaries on the top and the bottom.

$$\frac{dx_d}{dt} = u_{d,x}, \quad \frac{dy_d}{dt} = u_{d,y}, \quad \frac{du_{d,x}}{dt} = \frac{1}{r_d^2}\left(1 - u_{d,x}\right), \quad \frac{du_{d,y}}{dt} = -\frac{1}{r_d^2}u_{d,y},$$

$$\frac{dr_d^2}{dt} = -\delta, \quad \frac{dJ_{11}}{dt} = \omega_{11}, \quad \frac{dJ_{12}}{dt} = \omega_{12}, \quad \frac{dJ_{13}}{dt} = \omega_{13}, \quad \frac{dJ_{21}}{dt} = \omega_{21},$$

$$\frac{dJ_{22}}{dt} = \omega_{22}, \quad \frac{dJ_{23}}{dt} = \omega_{23}, \quad \frac{dJ_{31}}{dt} = 0, \quad \frac{dJ_{32}}{dt} = 0, \quad \frac{dJ_{33}}{dt} = \frac{\delta}{2r_d^2}J_{33},$$

$$\frac{d\omega_{11}}{dt} = -\frac{1}{r_d^2}\omega_{11} - \frac{2}{r_d^3}\left(1 - u_{d,x}\right)J_{31}, \quad \frac{d\omega_{12}}{dt} = -\frac{1}{r_d^2}\omega_{12} - \frac{2}{r_d^3}\left(1 - u_{d,x}\right)J_{32},$$

$$\frac{d\omega_{13}}{dt} = -\frac{1}{r_d^2}\omega_{13} - \frac{2}{r_d^3}\left(1 - u_{d,x}\right)J_{33}, \quad \frac{d\omega_{21}}{dt} = -\frac{1}{r_d^2}\omega_{21} + \frac{2}{r_d^3}u_{d,y}J_{31},$$

$$\frac{d\omega_{22}}{dt} = -\frac{1}{r_d^2}\omega_{22} + \frac{2}{r_d^3}u_{d,y}J_{32}, \quad \frac{d\omega_{23}}{dt} = -\frac{1}{r_d^2}\omega_{23} + \frac{2}{r_d^3}u_{d,y}J_{33}.$$

(19)

The initial conditions for System (19) are:

$$x_{d0} \in [-\epsilon, \epsilon], \quad y_{d0} = 0, \quad \epsilon = 0.05,$$

$$u_{d0,x} = 0.8\sin\left(\frac{\pi}{4}\frac{x_{d0}}{\epsilon}\right), \quad u_{d0,y} = 0.8\cos\left(\frac{\pi}{4}\frac{x_{d0}}{\epsilon}\right),$$

$$\widetilde{n}_d = \widetilde{n}_{d0}, \quad r_d = r_{d0}, \quad J_{11} = J_{22} = J_{33} = 1,$$

$$J_{12} = J_{13} = J_{21} = J_{23} = J_{31} = J_{32} = J_{33} = 0,$$

(20)

$$\omega_{110} = \frac{0.8}{\epsilon}\frac{\pi}{4}\cos\left(\frac{\pi}{4}\frac{x_{d0}}{\epsilon}\right), \quad \omega_{120} = \omega_{130} = 0,$$

$$\omega_{210} = -\frac{0.8}{\epsilon}\frac{\pi}{4}\sin\left(\frac{\pi}{4}\frac{x_{d0}}{\epsilon}\right), \quad \omega_{220} = \omega_{230} = 0.$$

As in the 1D case, the numerical calculations were verified using the analytical solution to System (19) (for the sake of space, the analytical solution is included in Appendix A; its derivation is trivial and similar to Solution (17)). Droplet trajectories, their sizes and distribution for the

case of $\delta = 1$ are presented in Fig. 3. It should be noted that, although in the 2D space the droplet trajectories intersect, there is no intersection in the extended space, when the droplet size is included in the set of dimensions. The droplet distribution function remained single-valued in this case. Fig. 3 (left) shows droplet trajectories, where the size of the markers corresponds to the droplet size and colour denotes the droplet distribution function. Total number density profiles at horizontal cross-sections at various distances from the injection are presented in Fig. 3 (right). At the injection line, the droplet distribution is step-like. Further away from the injection, the distribution becomes smoother and the interval with non-zero droplet concentration becomes wider as the spray expands. As the spray is injected into a cross-flow, the number density is not symmetrical with respect to the axis of injection, and the maximum is shifted to the right as the droplet cloud travels to the right in the cross-flow. As the droplets evaporate and disappear, the droplet total number density decreases as the distance from the injection increases.

4. Two-phase flow past a cylinder

In this section, the capabilities of the original and generalised FLA in the cases of steady and unsteady gas-droplet flow with and without evaporation of droplets are demonstrated by the simulation of a 2D two-phase flow past a cylinder. Both the original and generalised FLA were incorporated into OpenFOAM by modifying the Lagrangian tracking library. The modification in the code enables the calculation of Jacobians and the number densities along chosen trajectories.

4.1. Modelling of a gas flow past a cylinder

Fluid flow around a cylinder is a classical problem and is often used as a benchmark for computational fluid dynamics codes (Zdravkovich, 1997). Depending on the flow Reynolds number, various flow regimes may be observed, including symmetric stationary flow with attached recirculation zones and periodic flows (Batchelor, 1999).

The flow domain and some notations used in our simulations are shown in Fig. 4, $x \in [-l_{in}, l_{out}]$ and $y \in [-l_w, l_w]$, the origin of the Cartesian coordinate system is located in the centre of the circle. The length and velocity scales are chosen to be the radius of the cylinder and the free-stream velocity. The Reynolds number values, Re, used in this paper, are half of those in works where the diameter of the cylinder is used as the length scale, as in for example Batchelor (1999). The values of l_{in}, l_{out} and l_w are set at 20, 60, and 20, correspondingly. See Appendix D for the details of the study, where the domain size was examined to ensure that the boundaries were sufficiently far away to not affect the flow field.

The inlet velocity was normal to the inlet. The outlet velocity condition was set as zero-gradient. The inlet and outlet pressure were set as

zero-gradient and a fixed value of zero, respectively. On the cross-section of the cylinder wall, there was the no-slip condition for the velocity and the zero-gradient condition for pressure. There were periodic boundary conditions for the boundaries on the top and bottom.

Normally, in such a study of a flow past a cylinder, the inlet velocity is fixed to be equal to the free-stream velocity in the far field. In this work, to model the case of a periodic flow, a transient perturbation was deliberately introduced at the inlet at an initial stage to trigger the onset of vortex shedding. It is inevitable that an asymmetric flow field corresponding to vortex shedding will develop in a computation with a symmetric configuration, providing that Re is sufficiently large and the computational time is sufficiently long. It is known that the asymmetry in simulations stems from truncation errors of computational models. Thus, improving the spatial and temporal resolution, which increases the accuracy, delays the start of vortex shedding. An asymmetrical longitudinal disturbance of the inlet velocity introduced at the initial stage was reported to significantly reduce the computational time for generating the periodic flow field (Laroussi et al., 2014). The velocity at the inlet, $x = -l_{in}, y \in [-l_w, l_w]$, is defined as follows

$$\mathbf{u}_g(-l_{in}, y, t) = \begin{cases} (1 + ae^{-ct}\sin(ky), 0) & \text{for } t \leq 10, \\ (1, 0) & \text{for } t > 10. \end{cases} \quad (21)$$

Here a and k are the amplitude and wave number of the disturbance, and c is the damping parameter. Their values are chosen as

$$a = 0.2, \quad k = \frac{\pi}{10}, \quad c = 1.$$

As suggested in Laroussi et al. (2014), these values have an effect on the length of the computational time taken to start generating the periodic flow, but not the flow pattern itself.

For the carrier phase, pimpleFoam with a direct numerical solver was used, with the solver configured as suggested by Bayraktar et al. (2012). The computational mesh was constructed in such a way that its quality within the boundary layer around the cylinder could be defined explicitly. The details are included in Appendix B.

4.1.1. Modelling verification

In the literature, the drag and lift coefficients, C_d and C_l, and Strouhal number, St, are often used to validate a numerical model of a flow past a cylinder. After conversion to non-dimensional variables, in a two-dimensional computation, these parameters can be calculated as follows,

$$\begin{aligned} C_d(t) = F_d(t) = \int_S \mathbf{e}_x \cdot \mathbf{P} \cdot \mathbf{n} \, ds, \\ C_l(t) = F_l(t) = \int_S \mathbf{e}_y \cdot \mathbf{P} \cdot \mathbf{n} \, ds, \quad \text{St} = 2f, \end{aligned} \quad (22)$$

where

$$\mathbf{P} = -p\mathbf{I} + \frac{1}{\text{Re}} \left[\nabla \mathbf{u} + (\nabla \mathbf{u})^T \right].$$

Here F_d and F_l are the total drag and lift forces along the circumference, $\mathbf{e}_x$ and $\mathbf{e}_y$ are the unit vectors of x and y directions respectively, $\mathbf{n}$ is the unit normal to the circumference, f is the frequency of oscillations (the dimensional scale for frequency is U/L), which is determined using the Fast–Fourier–Transform method to the results of $C_l(t)$.

To ensure reliable and accurate results, the independence study for the time step and cell sizes was carried out. Details are included in Appendix C.

4.2. Modelling of two-phase flows

In the gas flow calculated using the setup described above, droplets are injected at $x_{d0} = -5$ and $y_{d0} \in [-2, 2]$ at the same speed as the gas flow. At this cross-section, the local gas velocity is almost the same as the

free-stream velocity. Hence, it is expected that there would be only slight quantitative change in results if injecting droplets at a location further away from the cylinder.

Both original and generalised FLAs were incorporated into Open-FOAM, and to achieve this the Lagrangian module was modified and coupled together with pimpleFoam. The implementation was verified using the analytical solution for potential flow around a cylinder (see the details in Appendix E).

In what follows, a total number of $N_y = 51$ initial locations is defined for $y_{d0} \in [-2, 2]$. In the case of polydisperse droplets, a total number of $N_s = 41$ samples of different initial r_{d0} are chosen for $r_{d0} \in [0.1, 4]$. Interaction of droplets with the cylinder is not considered, when reaching the surface of the cylinder, droplets are assumed to stick to it. The initial conditions for $J_{ij,0}$ and $\omega_{ij,0}$ in System (10) are:

$$\begin{aligned} J_{ij,0} = 1, \text{ for } i = j; \quad J_{ij,0} = 0, \text{ for } i \neq j; \\ \omega_{ij,0} = 0, \text{ for any } i, j. \end{aligned}$$

4.2.1. Mapping the Lagrangian variables onto the Eulerian coordinates

System (10) describes the distribution function $\widetilde{n}_d$ within a Lagrangian framework, which is a function of t and the initial states ($\mathbf{x}_{d0}$, r_{d0}). To allow analysis of the droplet concentration in space and time, the droplet parameters need to be mapped from the Lagrangian to the Eulerian coordinates. This transformation can be carried out using various interpolation techniques. The one used in this work is described below.

It is assumed that the droplet phase fields (for example velocity) are continuous with respect to the Lagrangian variables (x_{d0}, y_{d0}, r_{d0}), not just time t. Taking an example of a steady case, if we need to find the distribution function $\widetilde{n}_d(r_d)$ and total concentration n_d at a location $\mathbf{x}_p = (x_p, y_p)$, the following steps are followed:

(i) As it is a steady-state case, t is a parameter along a trajectory, then linear interpolation with respect to t is applied to every trajectory to find the values of the droplet location y_d when $x_d = x_p$. Alongside that, values of the droplet size r_d and the determinant of the Jacobian $det\mathbf{J}$ are calculated using the same interpolation.

(ii) Once the parameters are known at $x_d = x_p$, interpolation of all the droplet parameters in y direction is arranged by inversely interpolating $y_d(x_{d0}, y_{d0}, r_{d0}, t)|_{x_d=x_p}$ with respect to y_{d0}. Note that the Lagrangian variable, y_{d0}, is used in the interpolation, and it assumes the continuity of droplet parameters as functions of droplet Lagrangian variables. This step is completed for all r_{d0}.

(iii) Now all the parameters, including droplet sizes and corresponding Jacobian values, are known at the selected location $\mathbf{x}_p = (x_p, y_p)$. The distribution function $\widetilde{n}_d = 1/|det\mathbf{J}|$ is defined as a function of r_d. Then a trapezoidal integration scheme is used to find the total droplet number density n_d by integrating the Expression (12).

In the description above it was assumed that the droplet parameter fields are single-valued. Note, that droplet trajectory crossing does not necessarily lead to multivalued parameter fields within the Lagrangian space (see Section 3.2.2). In the study, it was observed that multivalued droplet parameter fields are formed, when droplets engage in recirculating motion. In this case, the data for various groups should be identified to ensure interpolation within each group and that it is consistent with the continuity assumption specified above. Thus, even where a multivalued parameter field leads to a discontinuous function of $\widetilde{n}_d$ with respect to r_d at the chosen location, the continuity is ensured for each group. The total droplet number density n_d is then the sum of number densities calculated for each droplet family. It should be noted that even in the case, when the droplet parameter field is single-valued, but the carrier phase flow is complex, for example flow around an obstacle, the dispersed phase field might loose continuity, for example, when some
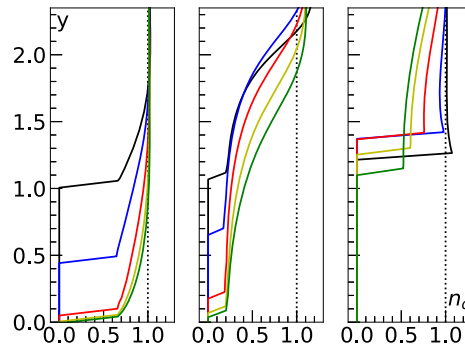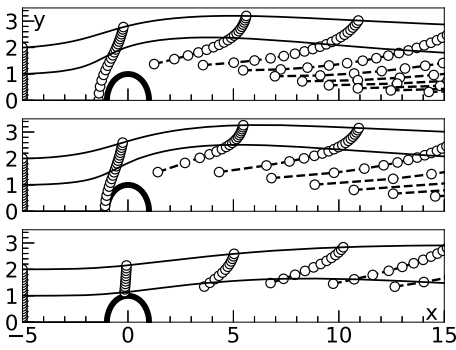
Fig. 5. Left: Trajectories of monodisperse non-evaporating particles injected at $x_0 = -5$ and $y_0 \in [0, 2]$ for $Stk = 0.1$ (top), 1 (middle) and 10 (bottom), $Re = 20$. The circular markers which are connected with broken lines tracks the same group of particles at the interval of $\Delta t = 5$. Solid lines represent the trajectories starting at $y_0 = 1$ and 2. Right: The droplet number density profiles at $x = 3, 6, 9, 12$ and 15, plotted in black, blue, red, yellow and green, respectively, for $Stk = 0.1$ (left), 1 (middle) and 10 (right). The dotted line is plotted as a reference line of $n_d = 1$. (For interpretation of the references to colour in this figure legend, the reader is referred to the web version of this article.)
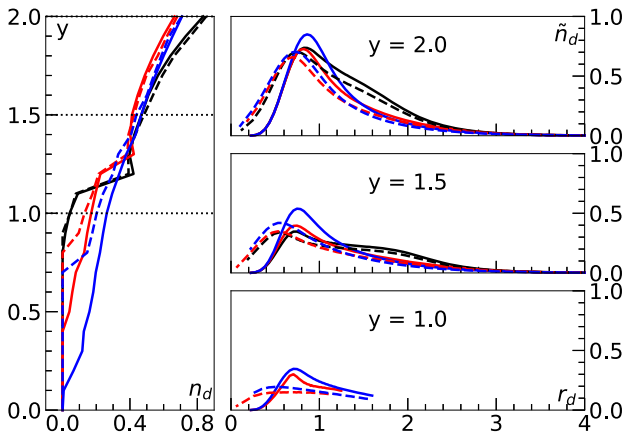

Fig. 6. Left: Total number density n_d profiles of a polydisperse spray along vertical cross-sections at $x = 3$ (black), 6 (red) and 9 (blue). Right: The distribution of number density $\tilde{n}_d$ vs. r_d when $x = 3$ (black), 6 (red) and 9 (blue) at the following vertical locations: $y = 2.0$ (top), 1.5 (middle) and 1.0 (bottom). Other parameters are: $Re = 20$; reference Stokes number is $Stk = 1$; $\delta = 0$ (solid lines) and 0.05 (broken lines). (For interpretation of the references to colour in this figure legend, the reader is referred to the web version of this article.)

droplets stick to an obstacle, but the droplets on either side of the obstacle continue the motion and fill the space behind the obstacle.

In the case of monodisperse droplets without evaporation, the same procedure is used without the need of calculating the distribution function and its integral (12). As for an unsteady case, it is no longer possible to apply interpolation along a trajectory as it would correspond to a different time instance. However, the general methodology can be applied if extended to include the time of injection of each individual droplet t_0. More discussion is provided in Section 4.4.2.

4.3. Steady-state flow around a cylinder at $Re = 20$

In this subsection, the simulation results of monodisperse and polydisperse droplet flow at $Re = 20$ are presented and discussed. The carrier phase flow is steady and symmetric with respect to $y = 0$, thus the trajectories and concentrations of droplets are symmetric as well.

4.3.1. The case of monodisperse droplets and non-evaporating conditions

We begin the discussion of the results with the simplest case of monodisperse droplet flow without evaporation. The focus is on how the droplet concentration field depends on the droplet sizes. This problem has been considered before. Healy and Young (2005) studied it in a potential flow. Zaripov et al. (2017) plotted concentration contours near the cylinder at a range of different values of Stk and Re. However, the

droplet concentration field in a steady flow has not been fully converted to the Eulerian framework.

Since there have been studies of this flow, only some results will be presented in this paper. Sample trajectories and deformation of a droplet cloud, which originally was set as a line at $x = -5$, are plotted as solid lines and circles connected by broken lines, respectively, for Stk $= 0.1$, 1 and 10, as shown in Fig. 5(left). Because of the symmetry, only the top half of the flow domain, $y \geq 0$, is shown. As expected, larger droplets, Stk $= 10$, have higher inertia and their trajectories are less deformed from straight lines, while smaller droplets, Stk $= 0.1$, follow the carrier phase streamlines more closely due to the viscous forces. More of the smaller droplets move around and past the cylinder rather than fall onto its surface. On the other hand, the cloud of smaller droplets deforms more and becomes longer than in the case of large droplets. In all cases, the droplets lagging furthest behind are the ones closest to $y = 0$.

Using the mapping described in Section 4.2.1, the profiles of droplet total number density at vertical cross-sections $x = 3, 6, 9, 12$ and 15 are plotted for the same droplet Stokes numbers, see Fig. 5(right). One can see that the regions devoid of droplets on this plot correspond to $n_d = 0$. The width or height of this region depends on the droplet size, and it is consistent with the trajectory map presented in the same figure on the left. The width/height of the empty region decreases, however not necessarily monotonically, downstream of the cylinder. At Stk $= 10$, it increases slightly from $x = 3$ to 9 and then decreases. The smaller size of the empty region corresponds to what of the smaller droplets. Another interesting result is that at Stk $= 1$, the total number density curves have smaller jumps at the boundary of the empty region.

4.3.2. Polydisperse droplets

Consider the injection of polydisperse droplets with reference value Stk $= 1$ and log-normal initial droplet distribution, as in Expression (11). The droplet size distribution is different at different locations. The reason for that is obvious from the results presented above in Section 4.3.1, the dispersed phase parameter fields depend on the droplet sizes.

Some results of the modelling are presented in Fig. 6; total number density profiles at $x = 3, 6$ and 9 are shown in the figure on the left, and droplet size distribution at 9 points in a rectangle $[3, 9] \times [1, 2]$ are shown in three figures on the right. Curves corresponding to the non-evaporating case, $\delta = 0$, are solid, while broken curves denote the evaporating case with $\delta = 0.05$. First, let us discuss the case of non-evaporating droplets, $\delta = 0$. The droplet size distributions look similar to each other and similar to the initial droplet size distribution (see Fig. 1) at the points furthest away from the axis of symmetry. This corresponds to the fact that the flow is less disturbed at $y = 2$ than at points nearer to the cylinder. However, the distribution function maximum is lower in comparison to the initial distribution and the maximum corresponds to lower r_d. Moving to locations $y = 1.5$, and $y = 1$, it can be seen that the distribution curves become flatter, and the maximum further shifts to smaller size droplets. At $y = 1$, and $x = 6, 9$,
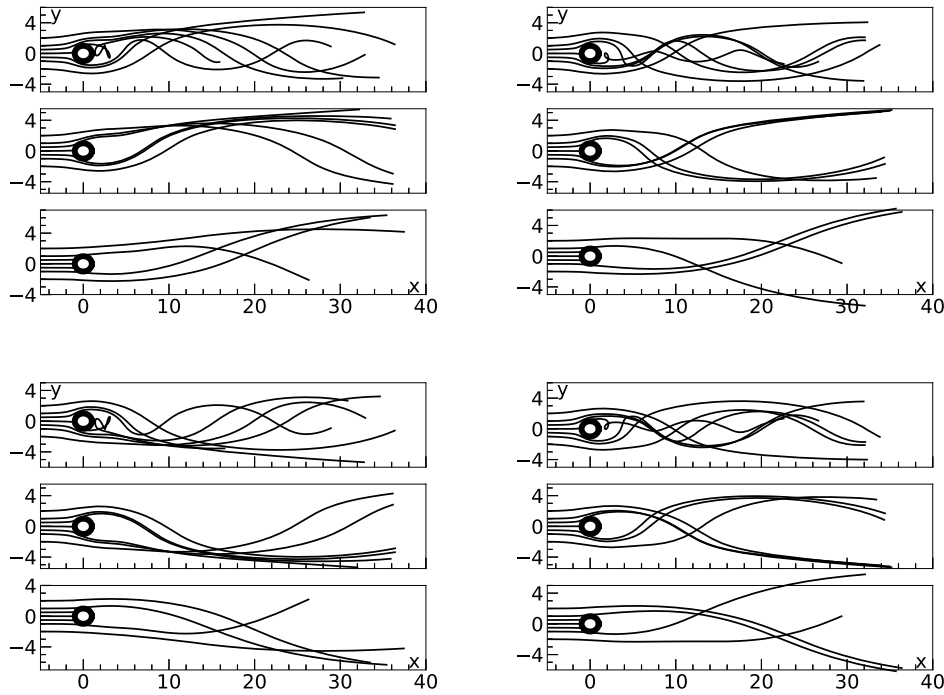
Fig. 7. Droplet trajectories plotted during their lifetime of 40, which are injected at $t_0 = 0$ (Top left), 2.5 (Top right), 5 (Bottom left) and 7.5 (Bottom right). Each figure contains three subplots for $Stk = 0.1$, 1 and 10 from top to bottom.
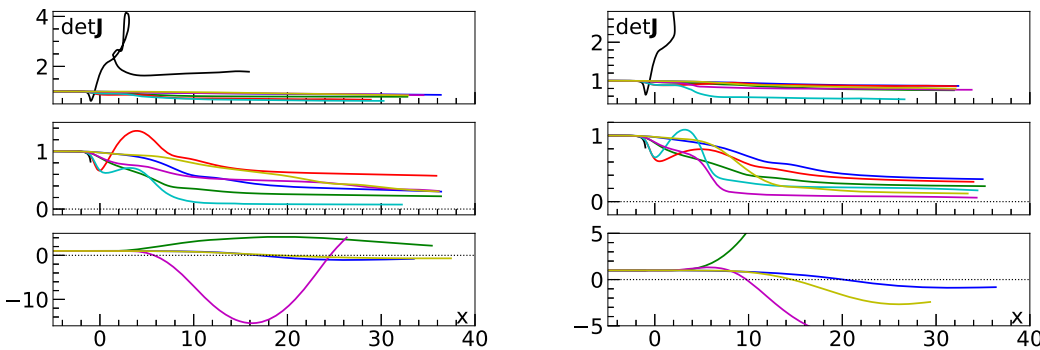

Fig. 8. The plots of $det\mathbf{J}$ versus x along the same droplet trajectories as presented in Fig. 7, which are injected at $t_0 = 0$ (left) and 2.5 (right). The colour denotes droplets injected at different initial locations: $y_{d0} = -2$ (blue), -1 (green), -0.5 (red), 0 (black), 0.5 (cyan), 1 (magenta), 2 (yellow). The thin dotted line represents $det\mathbf{J} = 0$. $Stk = 0.1$ (top), 1 (middle) and 10 (bottom). (For interpretation of the references to colour in this figure legend, the reader is referred to the web version of this article.)

the distribution function has its branch corresponding to large droplets cut, there are no large droplets travelling at this point. There are no droplets registered at point $(3,1)$. This observation is consistent with the findings discussed in Section 4.3.1, see Fig. 5 for $Stk = 1$ (middle figures).

The profiles of total number density concentration (see Fig. 6(left)), are consistent with those in the case of non-evaporating monodisperse droplets. As in the case for monodisperse droplets, the width/height of the empty region behind the cylinder reduces downstream. The total number density profiles increase with y, as the droplet cloud deforms and stretches. The total droplet number density is less than 1 near the $y = 0$ axis.

For comparison, the same group of results but for the case of evaporating droplets, $\delta = 0.05$, is presented on the same Fig. 6 with broken curves. As expected, evaporation leads to a shifting of the distribution curve maximum towards the smaller r_d and also reduced the value of the maximum $\widetilde{n}_d$ in comparison to the case for non-evaporating droplet. The empty region width/height is larger in comparison to the case for non-evaporating droplets because the small droplets, which travel closer to the symmetric plane, evaporate completely.

4.4. Results at Re = 100

In this section, a periodic unsteady gas-droplet flow is studied at Re = 100. As in the previous subsection, the results and discussions corresponding to monodisperse non-evaporating droplets are presented first, followed by those for polydisperse evaporating droplet. At Re = 100, the frequency of the periodic flow in the gas phase is found to be $f = 0.1$. This means that the period is $T = 10$.

4.4.1. Trajectories and $det|\mathbf{J}|$ of monodisperse droplets

As will be demonstrated later, in the case of vortex shedding, droplets engage in a circular vortex flow behind the cylinder, which develops and becomes wider further downstream.

The droplet trajectories for $Stk = 0.1$, 1 and 10, which are injected at four different times, $t_0 = 0, 2.5, 5, 7.5$, are shown in Fig. 7. The samples in the figure correspond to droplets injected at $y_{d0} = -2, -1, -0.5, 0, 0.5, 1$ and 2. The time interval between every two consecutive plots is equal to a quarter of the period ($T/4$). For convenience, the injection time instance of the first plot on the top left is denoted as $t_0 = 0$. The trajectories show more complicated dynamics for the droplet phase in comparison to the case at Re = 20. They include: circulation within, and then escape from, small regions; multiple intersections; and
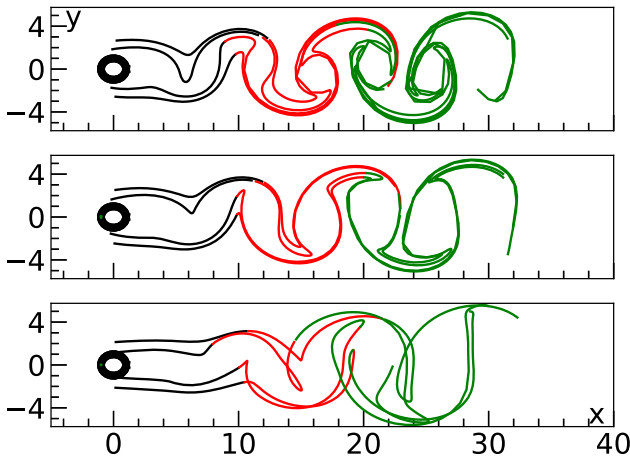
Fig. 9. A snapshot to track the locations of droplets which are injected between $t_0 \in [0, 10]$ at three time steps $t = 15$ (black), 25 (red) and 35 (green). The droplets starting at $y_{d0} = -2, -1, 1$ and 2 are tracked. It is equivalent to a snapshot at $t = 35$ of the droplets which are injected between $t_0 \in [0, 30]$. $Stk = 0.1$ (top), 1 (middle) and 10 (bottom). (For interpretation of the references to colour in this figure legend, the reader is referred to the web version of this article.)

congregation of various droplet trajectories. It should be noted that the intersection of two trajectories in an unsteady case does not necessarily lead to singularity in the droplet number density as it does in a steady case (Osiptsov, 1984). This is due to the fact that droplets may arrive at the intersection at different times.

Comparing droplet trajectories injected at $t_0 = 0$ and 5, it can be seen that the two plots are symmetric with respect to $y = 0$. The same applies to $t_0 = 2.5$ and 7.5 injection times. This indeed reflects the symmetric feature of gas flow; the vortex shedding is symmetric about $y = 0$ with a phase delay of $T/2$. Advantage can be taken of this fact to save computational costs.

The values of $det\mathbf{J}$ along the trajectories injected at $t_0 = 0$ and 2.5 are plotted in Fig. 8, noting that n_d is inversely proportional to the Jacobian's absolute value. The case of $det\mathbf{J} = 0$ implies an infinitely high number density n_d. It is interesting to note that the singularity in the number density field is observed at $Stk = 10$ but not $Stk = 0.1$, when even the more complicated intersection of trajectories is observed (see Fig. 7 (top)).

4.4.2. Transient traces of monodisperse droplets

Unlike in a steady case, in a transient case, droplet trajectories cannot be used to map droplet parameter fields (number densities included), to Eulerian coordinates at a chosen time instance. In contrast,

at a time instance t, $\mathbf{x}_d$ of all droplets and corresponding r_d and $\tilde{n}_d$ need to be considered within the entire domain. Thus, one can connect the location of all droplets from the same $(\mathbf{x}_{d0}, r_{d0})$ injected during the time interval between the first injection and t, and this will form a transient trace of droplets with the same initial state. From the traces, the interpolation scheme, which is explained in Section 4.2.1, can be applied, by simply changing the parameter t to the time of injection t_0.

It is realised that large number of droplets are required to fill in a large computational domain, with sufficiently small intervals Δt_0 between the start of each group of droplets (in the calculations, droplets are injected in vertical lines) to keep the 'trace' as filled in as possible for accurate interpolation. However, one can take advantage of the periodic and symmetric features of the flow to reduce the computational cost significantly. Because of the periodicity, for example, tracking the droplets injected during $t_0 \in [t_1, t_1 + T]$ for a duration of $t \in [t_1, t_2 + nT]$, where $t_2 \geq t_1$ and n is integer, can recover states of droplets injected during $t_0 \in [t_1, t_1 + nT]$ for a duration of $t \in [t_1 + nT, t_2 + nT]$. Furthermore, one only needs to inject droplets above the $y = 0$ axis (in our case $y_0 \in [0, 2]$), as the data on droplets injected below the axis can be reconstructed using symmetry and applying a phase delay of $T/2$.

An example of the application of this method is Fig. 9, which illustrates traces of droplets at $t = 35$ with the droplet injected during $t_0 \in [0, 30]$, when $Stk = 0.1$, 1 and 10. The traces are recovered from a simulation of droplets injected at $y_{d0} \in [0, 2]$ and $t_0 \in [0, 10]$ for a duration of $t \in [0, 40]$. Due to the periodicity, the traces of these droplets at $t = 15$, 25 and 35 can be superimposed which is equivalent to one set of traces at $t = 35$ of droplets injected at $y_{d0} \in [0, 2]$ and $t_0 \in [0, 30]$. Similarly, to visualise droplets injected in the bottom half, another set of traces is
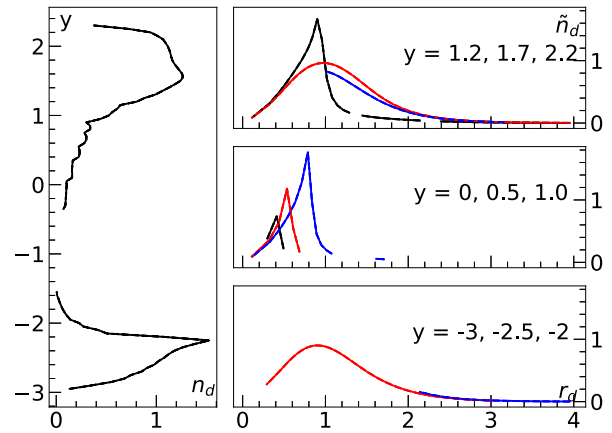

Fig. 11. The same distributions as in Fig. 10 (left), but for evaporating droplets, $\delta = 0.04$.
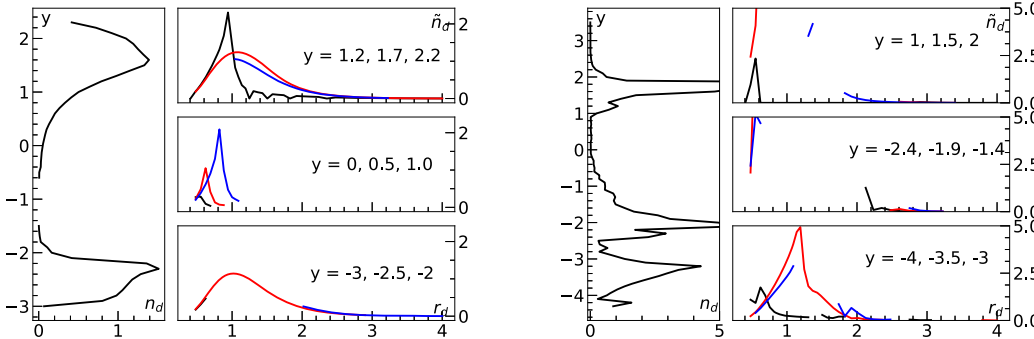

Fig. 10. Left: The total number density, n_d, profile at $x = 5$ (the vertical subplot) when $t = 35$ (Fig. 9) and the droplet size distribution at $x = 5$ and $y = 1.2$ (black), 1.7 (red) and 2.2 (blue), shown on the top subplot, $y = 0$ (black), 0.5 (red) and 1.0 (blue), shown on the middle subplot, $y = -3$ (black), -2.5 (red) and -2 (blue), shown on the bottom subplot. Right: The total number density n_d profile at $x = 15$ (the vertical subplot) and the droplet distribution at $x = 15$ and $y = 1$ (black), 1.5 (red) and 2 (blue), shown on the top subplot, $y = -2.4$ (black), -1.9 (red) and -1.4 (blue), shown on

the middle subplot, $y = -4$ (black), -3.5 (red) and -3 (blue), shown on the bottom subplot. Non-evaporating droplets. (For interpretation of the references to colour in this figure legend, the reader is referred to the web version of this article.)
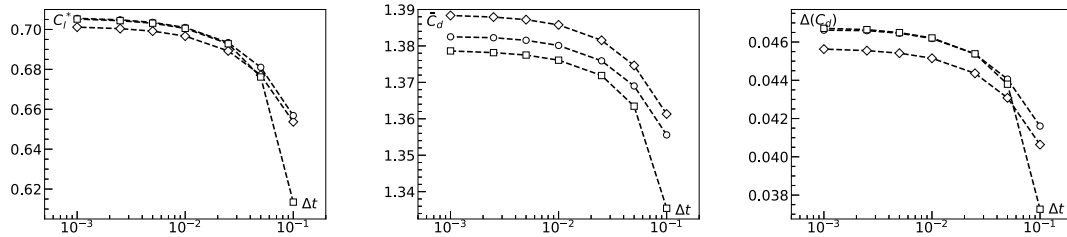
Fig. 12. Dependence of C_l^*, $\overline{C}_d$ and $\Delta(C_d)$ on Δt (left, middle and right, respectively). Square, circle and diamond markers denote $N_r = 3, 5, 10$, respectively (number of mesh layers within a boundary layer.
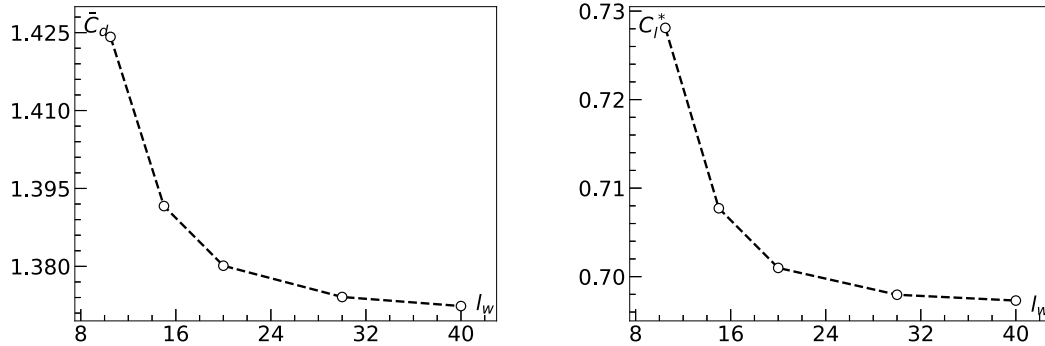

Fig. 13. Dependence of the mean drag coefficient $\overline{C}_d$ (left) and amplitude of the lift coefficient C_l^* (right) on l_w.
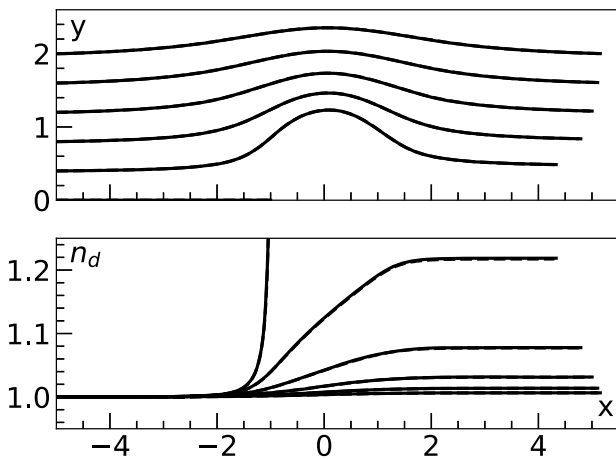

Fig. 14. Droplet trajectories (top) and droplet number density along chosen droplet trajectories (bottom), $Stk = 0.1$ and $\delta = 0.1$, potential flow around a cylinder. The droplets are injected at $x_{d0} = -5$ and $y_{d0} = 0, 0.2, 0.4, 0.6, 0.8, 1.0$. The curves with larger n_d values correspond to trajectories starting closer to the x-axis. Solid curves denote numerical results calculated using the modified OpenFOAM solver, broken curves denote results obtained using an in-house stand-alone code. The two groups of results match with each other perfectly, the broken curves are barely distinguishable.

generated at $t = 20, 30,$ and 40. This is due to the symmetry present with a phase delay of $T/2$. After changing the sign of y, it gives a set of traces starting from $y_{d0} \in [-2, 0)$ at $t = 15, 25,$ and 35.

As is apparent from Fig. 9, the traces show that the vortices in the gas flow have a significant clustering effect on the droplets, especially the small ones. Along the vortex street, the droplets are segregated, with the smaller droplets accumulating closer to the centres of the vortices. This segregation becomes more pronounced further downstream behind the cylinder. The droplets tend to collect in thin regions between adjacent vortices, from where they move along the periphery of a vortex away

from the axis while still accumulating within thin zones.

4.4.3. Number density distribution of polydisperse droplets

The distribution function $\tilde{n}_d$ and the total number density are much more complex than in the case without vortex shedding; this is caused by droplet size segregation; see the profiles and distributions at $x = 5$ and 15 in Fig. 10. At $x = 5$ (Fig. 10, left), only small droplets reach the region near $y = 0$ as shown in the middle of the three horizontal subplots. These droplets are injected at $y_0 > 0$ and brought closer to the axis by the vortex in the carrier phase, which is consistent with the traces shown in Fig. 9. For $y > 0$, away from the axis, the droplet population changes gradually from only small droplets, to a full spectrum of all sizes, then to only large droplets, as shown in the top subplot. For $y < 0$, if sufficiently far away from the axis, as shown in the bottom subplot, the droplet population varies from large droplets only to small droplets only following the decrease in y. According to the results presented in this subplot, small and medium-sized droplets injected in the bottom half, $y_0 < 0$, appear only at $y < -2$ at the cross-section $x = 5$ due to blockage of the cylinder and the vortices in the carrier phase flow, while the vertical locations of large droplets do not move away from their initial y_0 as much. The total number density n_d profile shows that its two local maxima are reached both above and below the x-axis and correspond to locations, where the droplet size spectrum is the fullest.

At $x = 15$, shown in Fig. 10 (right), the segregation is stronger. As can be seen in the three subplots of droplet size distribution $\tilde{n}_d$, only some size ranges, in some cases small, are observed at each of the chosen locations. For example, high densities ($\tilde{n}_d$ values are up to 5) of small droplets appear at $y = 1$ and 1.5, while at $y = 2$ the distribution has two pieces, one branch is short but high for mid-sized droplets, and another branch corresponds to large-sized droplets. The droplet distribution function $\tilde{n}_d$ is infinitely high for small droplets at $y = -1.9$ and 1.5. This leads to a singularity in the total number density n_d as well. Although not present in the distributions shown in Fig. 10, it is probable that an infinitely high value of $\tilde{n}_d$ corresponding to large droplets is present at a different location, this follows from Fig. 8. Note that an infinitely high number density value corresponds to a collapse of a Lagrangian element.

The singularity is integrable in this case, meaning that the number of droplets remains finite (Osiptsov, 1984). However, as the singularity may impose difficulties in accurately interpolating $\widetilde{n}_d$ and then calculating n_d without overburdening the computation, further investigation is required to justify the quantitative results of n_d around the singularity.

The same distributions but for the case of evaporating droplets with $\delta = 0.04$ are shown in Fig. 11. The distributions of $\widetilde{n}_d$ and the total number density profiles are plotted at the same locations as in Fig. 10 (left). Qualitatively the results are similar to the case of non-evaporating droplets $\delta = 0$, except that the values of the total number density n_d and distribution function $\widetilde{n}_d$ are lower due to the evaporation.

5. Conclusion

In this paper, a generalised FLA to describe polydisperse evaporating droplet flows is presented. The generalisation of the fully Lagrangian approach is based on the extension of the Lagrangian variable space to include droplet size. The paper includes a description of the mathematical formulation, methodology, details of key elements of implementation, and some examples of application. The examples presented involved a number of simplifying assumptions, for example the simple Stokes drag and the infinite heat conductivity model were used to describe the momentum and evaporation equations of the droplet phase. A log-normal function was employed to describe the droplet size distribution. However, these assumptions do not limit the application of the generalised FLA. Appropriate expressions for the momentum and energy exchange terms can be used for a specific application, as well as other forms of droplet size distribution functions.

The generalised FLA was applied to simple cases where the solution could be found analytically. These cases were used to verify the numerical implementation. Probably the most interesting finding of this exercise is that droplet trajectory crossing does not necessarily lead to multivalued droplet parameter fields. This is attributed to the fact that the variable domain is extended by including the droplet size.

To enable simulation of polydisperse droplets in more complex carrier fields, the generalised FLA was incorporated into OpenFOAM as a modified Lagrangian module, whilst the pimpleFoam module was used to calculate the gas flow field. A mapping procedure was suggested and implemented to convert the droplet parameter field from Lagrangian to Eulerian coordinates. This mapping is a processing tool, which enables better understanding of droplet distribution in space and and its change with time.

The presentation of the examples of the generalised FLA application has two parts. The first part shows simulation results of representative groups of monodisperse droplets. This is useful information that could be used as a reference for the case of polydisperse droplets. It could also be interpreted, if the results for all groups of monodisperse droplets are superimposed, as an approximation of the polydisperse droplet case. Simulation results for polydisperse droplets are discussed in the second part.

Gas-evaporating droplet flow past a circular cylinder was simulated as a benchmark case. Some key features of the droplet distribution in a steady and periodic laminar flow were captured. In the steady case, an empty region free of droplets can be clearly identified from the total number density profiles, which correspond to the picture of droplet trajectories. The droplet number density profiles give a better understanding of how droplets are distributed and how this distribution depends on droplet sizes. It is demonstrated that evaporation increases the size of the empty region because smaller droplets, which travel closer to the axis of symmetry in non-evaporating conditions, evaporate completely and disappear.

In the periodic case, the droplet trajectories are much more complex and include small recirculation zones. To study the number density profiles at a given time instance, a snapshot of all droplets and their states within the whole computational domain is used for analysis, assuming a constant injection of droplets. The obtained distribution profiles show droplet segregation by size, which becomes more pronounced further downstream. The droplet phase fields become multivalued in the extended Lagrangian space, with development of singularities in the droplet distribution function on the folds of the dispersed phase continuum, which in turn are reflected as infinitely high droplet total number densities at the same point. The singularity, however, is an artefact of the mathematical model corresponding to the collapse of the Lagrangian element. Usually, such singularities are integrable and correspond to a finite number of droplets as explained in Osiptsov (1984).

This work focuses on demonstration of the potential of the generalised FLA for studying both steady and unsteady polydisperse gas-droplet flows with or without evaporation. The developed methodology provides insight into droplet distribution in terms of size and space and their evolution with time in two-phase flows. Thus, it enables visualisation of droplet distribution in the computational domain. To the best of our knowledge, this is the first work to demonstrate such functionality in the family of Eulerian–Lagrangian gas-evaporating droplet simulation approaches. Post-processing is relatively straightforward in the case of single-valued droplet fields. In the case of strong droplet segregation and recirculation, the droplet distributions are much more complex and might contain singularities. This does not affect the simulation accuracy in the vicinity of the singularity or downstream, however further development is required for visualisation of the droplet distribution.

CRediT authorship contribution statement

Y. Li: Conceptualization, Methodology, Software, Validation, Investigation, Data curation, Writing – original draft, Writing – review & editing, Visualization, Project administration. **O. Rybdylova:** Conceptualization, Methodology, Software, Validation, Visualization, Writing – original draft, Writing – review & editing, Supervision, Project administration, Funding acquisition.

Declaration of Competing Interest

The authors declare that they have no known competing financial interests or personal relationships that could have appeared to influence the work reported in this paper.

Acknowledgements

Appendix A. Solution to system (19)

System (19) with initial conditions (20) can be solved analytically. Assuming $\delta \neq 0$ and $\delta \neq -1$, the solution is:

$$x_d = x_{d0} + t - \left(1 - u_{d0,x}\right)\frac{r_{d0}^2}{\delta + 1}\left[1 - \left(1 - \frac{\delta t}{r_{d0}^2}\right)^{(\delta+1)/\delta}\right],$$

$$y_d = u_{d0,y}\frac{r_{d0}^2}{\delta + 1}\left[1 - \left(1 - \frac{\delta t}{r_{d0}^2}\right)^{(\delta+1)/\delta}\right],$$

$$u_{d,x} = 1 - \left(1 - u_{d0,x}\right)\left(1 - \frac{\delta t}{r_{d0}^2}\right)^{1/\delta},$$

$$u_{d0,y} = u_{d0,y}\left(1 - \frac{\delta t}{r_{d0}^2}\right)^{1/\delta}, \quad r_d^2 = r_{d0}^2 - \delta t,$$

$$\frac{J_{11} - 1}{\omega_{110}} = \frac{J_{21}}{\omega_{210}} = \frac{r_{d0}^2}{\delta + 1}\left[1 - \left(1 - \frac{\delta t}{r_{d0}^2}\right)^{(\delta+1)/\delta}\right],$$

$$J_{22} = 1, \quad J_{12} = J_{31} = J_{32} = 0,$$

$$J_{33} = \left(1 - \frac{\delta t}{r_{d0}^2}\right)^{-1/2},$$

$$\frac{J_{13}}{1 - u_{d0,x}} = \frac{J_{23}}{-u_{d0,y}} = -\frac{2r_{d0}}{\delta}\left[\frac{1}{1+\delta}\left(1 - \frac{\delta t}{r_{d0}^2}\right)^{1/\delta+1} - \left(1 - \frac{\delta t}{r_{d0}^2}\right)^{1/\delta} + \frac{\delta}{(1+\delta)}\right],$$

$$\frac{\omega_{11}}{\omega_{110}} = \frac{\omega_{21}}{\omega_{210}} = \left(1 - \frac{\delta t}{r_{d0}^2}\right)^{1/\delta}, \quad \omega_{12} = \omega_{22} = 0,$$

$$\frac{\omega_{13}}{1 - u_{d0,x}} = \frac{\omega_{23}}{-u_{d0,y}} = \frac{2}{\delta r_{d0}}\left[\left(1 - \frac{\delta t}{r_{d0}^2}\right)^{1/\delta} - \left(1 - \frac{\delta t}{r_{d0}^2}\right)^{1/\delta-1}\right].$$

(23)

Appendix B. Mesh design

The meshing structure for problem simulations of this kind is often designed with fine grids close to the cylinder, their size increasing gradually towards the other boundaries (see for example Bayraktar et al., 2012; Zaripov et al., 2017). Indeed, the region near the cylinder requires a better resolution because of the boundary layer formation. Although mesh independence tests were carried out in the cited works in terms of the total number of cells, it remains unclear what element size is sufficient near the cylinder. In this work, the quality of mesh is defined differently and based on the size of cells closest to the cylinder.

The mesh quality is quantified by the mesh resolution with respect to the boundary layer, and is a measure of the ability to capture the essential physics. It is well known that the thickness of a boundary layer is proportional to $Re^{-1/2}$ (Schlichting and Gersten, 2016). Thus, $Re^{-1/2}$ is taken as a reference value when describing the boundary layer thickness. Near the cylinder, cells are arranged in layers with inflation, and the number of annular layers is denoted by N_r within the $Re^{-1/2}$-layer in the radial direction. The size of the cells in the first layer near the cylinder in the radial direction is then $\epsilon_r = Re^{-1/2}(1-a)/(1-a^{N_r-1})$, where a is a defined geometric progression ratio. The arc length of a cell along the circumference of the cylinder is expected to be similar in size to the cell size in the radial direction. Thus the number of cells within each annular layer can be defined as $N_a = 4[\pi/(2\epsilon_r)]$. The square bracket denotes the integer part. This choice of N_a ensures a symmetric mesh design with the same number of cells in every quarter. The cell arc length along the cylinder circumference is $\epsilon_a = 2\pi/N_a$.

In our work, the mesh was created and validated only for the maximum value of Re used in our examples, which was $Re = 100$.

Appendix C. Time step and mesh independence study

The independence of the simulation results from the time step and mesh sizes is studied with respect to the drag and lift coefficients, C_d and C_l, and the Strouhal number, St, at $Re = 100$.

The values of the lift and drag coefficients, C_d and C_l, oscillate over time. Thus the mean value of C_d and the amplitude of C_d and C_l, which are denoted as $\overline{C}_d$, $\Delta(C_d)$ and C_l^*, are considered in the study. The mean value of C_l is zero.

The dependence of the results on the time step size, Δt, is shown in Fig. 12. According to this figure an acceptable accuracy is achieved with $\Delta t = 0.01$.

In all of these tested cases, the Strouhal number is $St = 0.2$.

The effect of the mesh size within the boundary layer is demonstrated in the same Fig. 12 using square, circle and diamond markers denoting $N_r = 3, 5, 10$, respectively. The simulation results are of acceptable accuracy when $N_r = 5$.

Appendix D. Validation study of the effect of the domain size

Three parameters describing the domain size were studied, namely l_{in}, l_{out} and l_w (see Fig. 4).

The results of the simulation, when the effect of l_w was studied, are presented in Fig. 13 (see plots of $\overline{C}_d$ and C_l^* vs. l_w). According to these figures, $l_w = 20$ is a good choice in that $\overline{C}_d$ and C_l^* only decrease by 0.06% and 0.04% respectively if the width is doubled, but by 1.33% and 1.17% if the width is reduce to $l_w = 10$. The amplitude of C_d is 0.045 with negligible variation.

A similar procedure was used to study the effect of the other two parameters. It was found that $l_{in} = 20$ and $l_{out} = 60$ are sufficiently large to apply

the far-field boundary conditions.

It should be noted that $N_r = 5$ was used for the calculations described above, and that the Strouhal number has the same value, $\text{St} = 0.2$, in all of these cases.

Appendix E. Verification of the Lagrangian module

A useful test case to validate the implementation of the fully Lagrangian approach (FLA) is to consider a potential flow around a cylinder with an analytical solution for the carrier phase (Healy and Young, 2005), in which the non-dimensional velocity potential can be written as

$$\phi_g = x + \frac{x}{x^2 + y^2}. \tag{24}$$

Then the x and y velocity components are

$$
\begin{aligned}
u_{g,x} &= \frac{\partial \phi_g}{\partial x} = 1 + \frac{y^2 - x^2}{\left(x^2 + y^2\right)^2}, \\
u_{g,y} &= \frac{\partial \phi_g}{\partial y} = -\frac{2xy}{\left(x^2 + y^2\right)^2}.
\end{aligned}
\tag{25}
$$

Therefore, the velocity derivatives, which are used in the FLA, are

$$
\begin{aligned}
\frac{\partial u_{g,x}}{\partial x} &= \frac{-2x(3y^2 - x^2)}{\left(y^2 + x^2\right)^3}, \quad \frac{\partial u_{g,x}}{\partial y} = \frac{2y(3x^2 - y^2)}{\left(y^2 + x^2\right)^3}, \\
\frac{\partial u_{g,y}}{\partial x} &= \frac{\partial u_{g,x}}{\partial y}, \quad \frac{\partial u_{g,y}}{\partial y} = -\frac{\partial u_{g,x}}{\partial x}
\end{aligned}
\tag{26}
$$

These expressions (25) were used with the equation of motion in the droplet phase, (10). The ODEs to find $\mathbf{x}_d$, $\mathbf{u}_d$ and the Jacobian components were solved using the 4th order Runge–Kutta method, then the number density n_d is found along trajectories using Eq. (8).

This verification was combined with the evaporation model (14), with evaporation coefficient $\delta = 0.1$. The droplets with $\text{Stk} = 0.1$ were injected at a number of selected points at $x_{d,0} = -5$ with the same initial velocity as the carrier phase.

The other initial conditions were

$$
\begin{aligned}
n_{d0} &= 1, \quad J_{11} = J_{11} = 1, \quad J_{12} = J_{21} = 0, \\
\omega_{11} &= \omega_{12} = \omega_{21} = \omega_{22} = 0.
\end{aligned}
\tag{27}
$$

For the purpose of verification of the modified Lagrangian module in OpenFOAM, it was coupled with potentialFoam, which computed the carrier phase velocity field. The boundary conditions at the cylinder surface were set for the slip condition instead of the standard no-slip. The reference data was calculated using in-house code for the 4th order Runge–Kutta method of integrating droplet parameters along their trajectories. Perfect agreement was achieved between the two sets of results, as shown in Fig. 14.

References

Almeida, T., Jaberi, F., 2006. Direct numerical simulations of a planar jet laden with evaporating droplets. Int. J. Heat Mass Transf. 49 (13-14), 2113–2123.

Batchelor, G.K., 1999. An introduction to Fluid Dynamics. Cambridge University Press, Cambridge, U.K. New York, NY.

Bayraktar, E., Mierka, O., Turek, S., 2012. Benchmark computations of 3D laminar flow around a cylinder with CFX, OpenFOAM and FeatFlow. Int. J. Comput. Sci. Eng. 7 (3), 253.

Begg, S., Kaplanski, F., Sazhin, S., Hindle, M., Heikal, M., 2009. Vortex ring-like structures in gasoline fuel sprays under cold-start conditions. Int. J. Eng. Res. 10 (4), 195–214.

Bourouiba, L., Dehandschoewercker, E., Bush, J., 2014. Violent expiratory events: on coughing and sneezing. J. Fluid Mech. 745, 537–563.

Crowe, C., Schwarzkopf, J., Sommerfeld, M., Tsuji, Y., 2011. Multiphase Flows with Droplets and Particles. Taylor & Francis Inc.

Dagan, Y., Greenberg, J., Katoshevski, D., 2017. Similarity solutions for the evolution of polydisperse droplets in vortex flows. Int. J. Multiph. Flow 97, 1–9. https://doi.org/10.1016/j.ijmultiphaseflow.2017.07.014.

Dolovich, M., Dhand, R., 2011. Aerosol drug delivery: developments in device design and clinical use. Lancet 377 (9770), 1032–1045.

Dunbar, L., Courtney, J., McMillen, L., 1975. Heating augmentation in erosive hypersonic environments. AIAA J. 13 (7), 908–912.

Fernandez, J., de la Mora, Rosner, D., 1981. Inertial deposition of particles revisited and extended: Eulerian approach to a traditionally Lagrangian problem. Physico-Chemical Hydrodyn. 2, 1–21.

Greenberg, J., Katoshevski, D., 2016. Polydisperse spray diffusion flames in oscillating flow. Combust. Theory Model. 20 (2), 349–372.

Greenberg, J., Silverman, I., Tambour, Y., 1993. On the origins of spray sectional conservation equations. Combust. Flame 93 (1-2), 90–96.

Healy, D., Young, J., 2005. Full Lagrangian methods for calculating particle concentration fields in dilute gas-particle flows. Proc. R. Soc. A 461 (2059), 2197–2225.

Karchniwy, E., Klimanek, A., Haugen, N., 2019. The effect of turbulence on mass transfer rates between inertial polydisperse particles and fluid. J. Fluid Mech. 874, 1147–1168.

Laroussi, M., Djebbi, M., Moussa, M., 2014. Triggering vortex shedding for flow past circular cylinder by acting on initial conditions: a numerical study. Comput. Fluids 101, 194–207.

Laurent, F., Massot, M., 2001. Multi-fluid modelling of laminar polydisperse spray flames: origin, assumptions and comparison of sectional and sampling methods. Combust. Theory Model. 5 (4), 537–572.

Laurent, F., Massot, M., Villedieu, P., 2004. Eulerian multi-fluid modeling for the numerical simulation of coalescence in polydisperse dense liquid sprays. J. Comput. Phys. 194 (2), 505–543.

Marble, F., 1970. Dynamics of dusty gases. Annu. Rev. Fluid Mech. 2 (1), 397–446.

Nguyen, T., Laurent, F., Fox, R., Massot, M., 2016. Solution of population balance equations in applications with fine particles: mathematical modeling and numerical schemes. J. Comput. Phys. 325, 129–156.

Osiptsov, A., 1984. Investigation of regions of unbounded growth of the particle concentration in disperse flows. Fluid Dyn. 19 (3), 378–385.

Osiptsov, A., 2000. Lagrangian modelling of dust admixture in gas flows. Astrophys. Space Sci. 274 (1/2), 377–386.

Panão, M., Moreira, A., 2004. Experimental study of the flow regimes resulting from the impact of an intermittent gasoline spray. Exp. Fluids 37 (6), 834–855.

Papoutsakis, A., Rybdylova, O., Zaripov, T., Danaila, L., Osiptsov, A., Sazhin, S., 2018. Modelling of the evolution of a droplet cloud in a turbulent flow. Int. J. Multiph. Flow 104, 233–257.

Rybdylova, O., Osiptsov, A., Sazhin, S., Begg, S., Heikal, M., 2016. A combined viscous-vortex, thermal-blob and Lagrangian method for non-isothermal, two-phase flow modelling. Int. J. Heat Fluid Flow 58, 93–102.

Rybdylova, O., Sazhin, S., Osiptsov, A., Kaplanski, F., Begg, S., Heikal, M., 2018. Modelling of a two-phase vortex-ring flow using an analytical solution for the carrier phase. Appl. Math. Comput. 326, 159–169.

Schlichting, H., Gersten, K., 2016. Boundary-Layer Theory. Springer-Verlag GmbH.

Tambour, Y., 1984. Vaporization of polydisperse fuel sprays in a laminar boundary layer flow: a sectional approach. Combust. Flame 58 (2), 103–114.

Tambour, Y., 1985. A Lagrangian sectional approach for simulating droplet size distribution of vaporizing fuel sprays in a turbulent jet. Combust. Flame 60 (1), 15–28.

Zaripov, T., Gilfanov, A., Begg, S., Rybdylova, O., Sazhin, S., Heikal, M., 2017. The fully Lagrangian approach to the analysis of particle/droplet dynamics: implementation into ANSYS FLUENT and application to gasoline sprays. At. Sprays 27 (6), 493–510.

Zaripov, T., Rybdylova, O., Sazhin, S., 2018. A model for heating and evaporation of a droplet cloud and its implementation into ANSYS Fluent. Int. Commun. Heat Mass Transf. 97, 85–91.

Zdravkovich, M.M., 1997. Flow Around Circular Cylinders: A Comprehensive Guide Through Flow Phenomena, Experiments, Applications, Mathematical Models, and Computer Simulations. Oxford University Press.